Pronounced Size Dependence in Structure and Morphology of Gas-Phase Produced, Partially Oxidized Cobalt Nanoparticles under Catalytic Reaction Conditions

Stephan Bartling,[*,†,△] Chunrong Yin,[‡,△] Ingo Barke,[*,†] Kevin Oldenburg,[†] Hannes Hartmann,[†] Viola von Oeynhausen,[†] Marga-Martina Pohl,[¶] Kelly Houben,[§] Eric C. Tyo,[‡] Sönke Seifert,[∥] Peter Lievens,[§] Karl-Heinz Meiwes-Broer,[†] and Stefan Vajda[‡,⊥,#,@]

[†]Institut für Physik, Universität Rostock, Universitätsplatz 3, D-18051 Rostock, Germany, [‡]Materials Science Division, [∥]X-ray Science Division, and [⊥]Center for Nanoscale Materials, Argonne National Laboratory, 9700 South Cass Avenue, Argonne, Illinois 60439, United States, [¶]Leibniz-Institut für Katalyse e.V. an der Universität Rostock (LIKAT), Albert-Einstein-Strasse 29a, D-18059 Rostock, Germany, [§]Laboratory of Solid-State Physics and Magnetism, KU Leuven, Celestijnenlaan 200d, Box 2414, 3001 Leuven, Belgium, [#]Department of Chemical and Environmental Engineering, Yale University, 10 Hillhouse Avenue, New Haven, Connecticut 06520, United States, and [@]Institute for Molecular Engineering, The University of Chicago, 5801 South Ellis Avenue, Chicago, Illinois 60637, United States. [△]S.B. and C.Y. contributed equally to this work.

ABSTRACT It is generally accepted that optimal particle sizes are key for efficient nanocatalysis. Much less attention is paid to the role of morphology and atomic arrangement during catalytic reactions. Here, we unravel the structural, stoichiometric, and morphological evolution of gas-phase produced and partially oxidized cobalt nanoparticles in a broad size range. Particles with diameters between 1.4 and 22 nm generated in cluster sources are size selected and deposited on amorphous alumina (Al_2O_3) and ultrananocrystalline diamond (UNCD) films. A combination of different techniques is employed to monitor particle properties at the stages of production, exposure to ambient conditions, and catalytic reaction, in this case, the oxidative dehydrogenation of cyclohexane at elevated temperatures. A pronounced size dependence is found, naturally classifying the particles into three size regimes. While small and intermediate clusters essentially retain their compact morphology, large particles transform into hollow spheres due to the nanoscale Kirkendall effect. Depending on the substrate, an isotropic (Al_2O_3) or anisotropic (UNCD) Kirkendall effect is observed. The latter results in dramatic lateral size changes. Our results shed light on the interplay between chemical reactions and the catalyst's structure and provide an approach to tailor the cobalt oxide phase composition required for specific catalytic schemes.

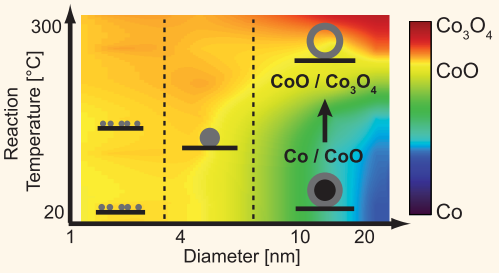

KEYWORDS: Co clusters and nanoparticles · oxidative dehydrogenation of cyclohexane · Kirkendall effect · cluster source · nanocatalysis · oxidation · surface deposition

Nanoparticles composed of noble metals like ruthenium, rhodium, gold, and platinum can act as efficient catalysts for a variety of chemical reactions.[1−5] Due to relatively high costs and limited resources, the use of more abundant metals is subject to intense research efforts in this field. For the production of liquid hydrocarbons in the Fischer−Tropsch synthesis transition metals, cobalt, in particular, is used as the standard catalyst of choice.[6−8] An open question remains as to the role of cluster size in the evolution of the particles' structure and morphology during reaction and the size-dependent interaction with the substrate.[9,10]

In recent publications, the behavior of nanoscale cobalt oxides has come into focus. Nanocrystalline cobalt monoxide (CoO), for example, can act as an efficient photocatalyst for solar water-splitting.[11] On the other hand, Co_3O_4 particles are efficient and selective catalysts for the oxidative dehydrogenation of cyclohexane[12−14] ($C_6H_{12} + (x/2)O_2 \rightarrow C_6H_{12-2x} + xH_2O$), which is a key step in chemical industry, *e.g.*, for the production of nylon.[15−17] These studies hint toward the

* Address correspondence to stephan.bartling@uni-rostock.de, ingo.barke@uni-rostock.de.

Received for review February 4, 2015 and accepted June 1, 2015.

Published online June 01, 2015
10.1021/acsnano.5b00791

important role of both cobalt particle size, as well as its oxidation state in determining catalytic activity and selectivity.

A crucial ingredient to unravel the precise mechanism of catalytic activity is the understanding of the evolution of the particles' properties during reaction. For Co, Fe, Al, Cu, Zn, and Ni, hollow spheres are commonly observed.[18−21] They are formed due to the nanoscale Kirkendall effect which describes the diffusion of material due to concentration gradients.[22−24] This can be used as a fabrication route to design nanotubes and hollow nanoparticles.[25] Detailed studies of the formation of hollow cobalt nanocrystals through the Kirkendall effect in solution are available in the literature.[18,26] Supported Co nanoparticles that have been prepared by Chernavskii et al. in solution show the formation of hollow spheres upon oxidation[27] as well as particles deposited at the water−air interface.[28] The latter are reported to undergo the morphologic change already at room temperature. Some studies hint at a crucial role of the Kirkendall effect for the catalytic mechanism, for instance, for the specific case of Co redispersion in cobalt Fischer−Tropsch catalyst regeneration.[29−32]

The main goal of this work is to follow the evolution of the oxidation state and morphology of supported size-selected and partially oxidized Co clusters during the oxidative dehydrogenation of cyclohexane, thus linking the particle properties to available chemical studies.[12] The clusters are produced by gas aggregation representing a physical method that avoids the formation of ligands or protective layers at the particles' surface. Subsequent soft landing on Al_2O_3 and UNCD substrates takes place under high vacuum conditions. The actual reaction experiments are conducted in a setup for temperature-programmed reactions (TPRx) to mimic realistic conditions. A combination of different experimental methods is applied to determine changes in stoichiometry, structure, size, shape, and influence of the substrate. *In situ* grazing incidence small-angle X-ray scattering (GISAXS) and grazing incidence X-ray absorption near edge structure (GIXANES) serve to show size- and support-dependent changes in morphology and chemical state under realistic reaction conditions as a function of reaction temperature. *Ex situ* methods like reflection high energy electron diffraction (RHEED) and transmission electron microscopy (TEM) are employed to determine the stoichiometry, size, and shape of the clusters before and after the catalytic reaction.

EXPERIMENTAL RESULTS AND DISCUSSION

An overview of the investigated samples in this work is given in Table 1. The mean initial and final cluster diameters (d_i and d_f) are mainly determined by TEM, and the samples are named "*i*" before and "*f*" after the oxidative dehydrogenation of cyclohexane, respectively.

TABLE 1. List of Samples Used in This Work[a]

sample ID	substrate	d_i (nm) (before reaction)	d_f (nm) (after reaction)
L1i/f	Al_2O_3	(15 ± 2)	(15 ± 3)
L2i/f	Al_2O_3	(22 ± 5)	(24 ± 5)
L3i/f	UNCD	(21 ± 8)	(30 ± 9)
M1i/f	Al_2O_3	(4.4 ± 0.6)	(4.1 ± 0.6)
M2i/f	UNCD	4*	
S1i/f	Al_2O_3	2*	
S2i/f	UNCD	2*	
S3i/f	Al_2O_3	1.4*	

[a] The samples are named "*i*" (initial) before reaction and "*f*" (final) after the oxidative dehydrogenation of cyclohexane in the TPRx experiment. The mean initial and final outer cluster diameters (d_i and d_f) are measured by TEM. Numbers marked by an asterisk are determined by atomic force microscopy (AFM) and are not directly comparable to the TEM data. Before reaction, large particles (samples "L") have a core-shell structure, whereas the intermediate ("M") and small ("S") clusters are fully oxidized due to air exposure.

We classify the samples into three groups based on the size regime. These are large clusters (L1−L3) with a diameter larger than 10 nm, intermediate clusters (M1−M2) with diameters around 4−5 nm, and small clusters (S1−S3) around 2 nm. In the following text, we elaborate on the size-dependent composition and morphological behavior of the clusters under reaction conditions of the oxidative dehydrogenation of cyclohexane. We note that for the subsequent results the presence of cyclohexane is expected to have only a minor effect on the particles' properties due to the high oxygen content in the gas environment (see the Discussion and Methods). Thus, the following results are expected to be of relevance in other oxidative reactions as well.

Large Clusters. Figure 1a shows a typical evolution of *in situ* GIXANES spectra of large clusters on Al_2O_3 (L1) under reactive conditions with increasing temperature from initially 25 °C up to 300 °C and subsequent cooling to room temperature (see the Methods). The onset of spectral changes appears at 150 °C where the first peak at 7726 eV becomes more prominent and a second peak at higher energies emerges. An additional pronounced change in the spectra can be observed from 250 to 300 °C where the shape and position of the first peak is altered. Cooling back to room temperature does not lead to any further changes. This hints to a non-reversible composition change of the deposited Co clusters during the treatment. Each spectrum is evaluated through linear combination analysis, in which a best fit spectrum is acquired utilizing reference samples to determine partial contributions that make up the composition of the experimental sample. The best fit for the current cobalt samples results from contributions of metallic Co, CoO, and Co_3O_4 (Figure 1b) reflecting the most expected oxidation states of Co, as previously reported.[9,33−36] The result of the linear combination analysis, in an oxygen-rich environment, is shown in Figure 1c, where the contribution of each reference to a single spectrum is

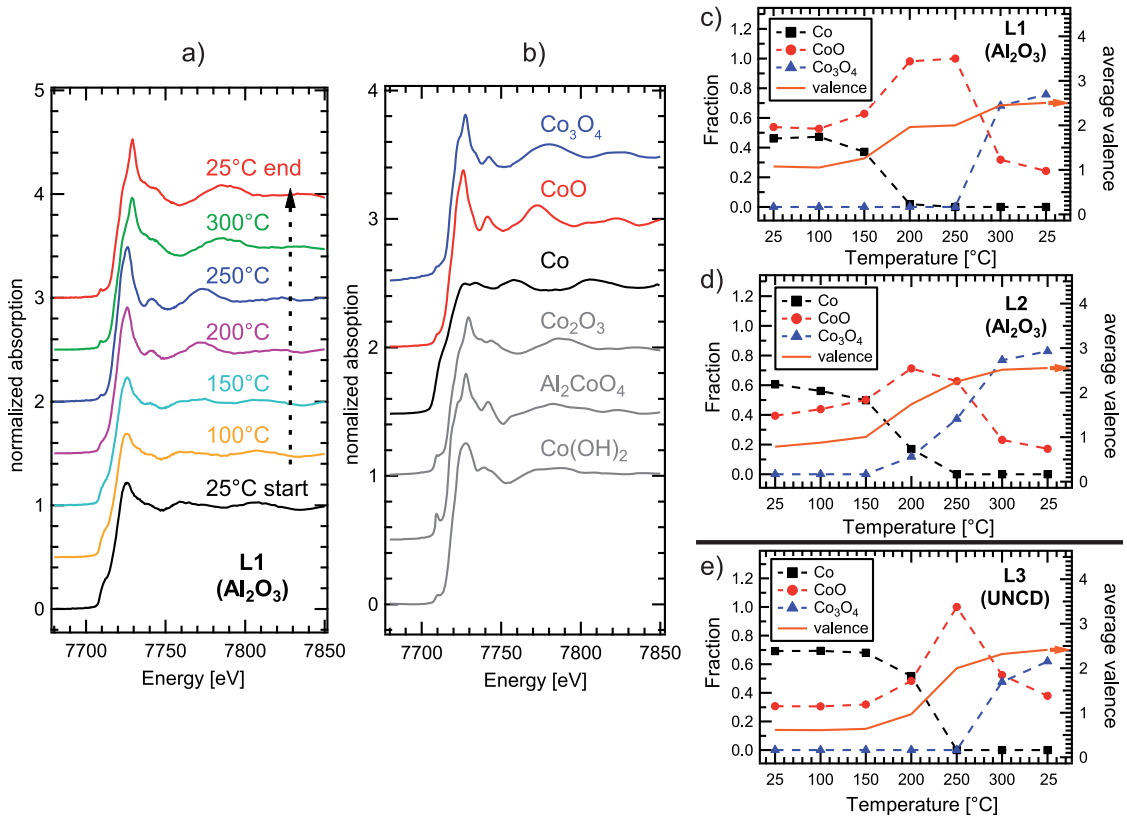

Figure 1. *In situ* **GIXANES results from large clusters under reactive conditions. (a) Normalized GIXANES spectra on Al_2O_3 (L1, d_i = 15 nm) at different temperatures. The spectra are offset vertically for clarity. (b) Reference spectra used for quantitative determination of sample composition by fitting a linear combination of metallic Co (black), CoO (red), and Co_3O_4 (blue) to the curves in (a). Compounds not contained in spectra are shown in gray for comparison. (c–e) Composition of clusters on sample L1 (c), L2 (d_i = 22 nm) (d), and L3 (d_i = 21 nm) (e) during the TPRx experiment, revealing the oxidation of elemental Co (black squares) to CoO (red circles) and to Co_3O_4 (blue triangles) at higher temperatures. The deduced averaged valence (solid orange curve) represents the oxidation state of the Co particles.**

plotted *versus* temperature along with the resulting averaged valence representing the averaged oxidation state. The oxidation state of cobalt in each reference is determined by multiplying the number of oxygen atoms by −2 (the oxidation state of oxygen) then dividing by the number of cobalt atoms, the product is multiplied by −1 to balance charge. The average oxidation state of the sample is determined by multiplying the oxidation state of each reference by the compositional fraction and summing all values. From this analysis the initial particle composition at the beginning of the TPRx experiment appears to be 45% metallic cobalt and 55% CoO. The particles are deposited as pure Co clusters but become oxidized when they are transferred through air from the cluster deposition apparatus to the reaction cell. Starting at about 100 °C more of the metallic Co (valence 0) is converted to CoO (valence 2). The CoO fraction reaches a maximum at about 250 °C and is then further oxidized to Co_3O_4 (valence $2^2/_3$). The course of oxidation is characterized by the averaged valence (solid curve), a convenient measure for the evolution of the oxidation of the particle ensemble. At the end of the treatment, the clusters have an averaged valence of about 2.5 and consist of about 25% CoO and 75% Co_3O_4. For even larger clusters on Al_2O_3 (L2, d_i = 22 nm, see Figure 1d), the general behavior is similar except for some differences in the initial state (60% metallic Co) and at the end of the treatment (85% Co_3O_4).

On UNCD, the clusters with an initial size of 21 nm (L3) show the highest metallic Co amount after air exposure. During the TPRx experiment they start to convert to CoO at slightly higher temperatures compared to L1 and L2 (*i.e.*, on Al_2O_3); see averaged valence in Figure 1e. Accordingly, the composition of these particles after the reaction is 40% CoO and 60% Co_3O_4. The averaged valence is about 2.4 and thus slightly lower compared to L1 in (c) and L2 in (d).

In addition to GIXANES under reactive conditions, RHEED measurements are conducted in ultrahigh vacuum (UHV) to determine the composition of the treated and untreated particles by an alternative method which relies on crystallographic properties. The RHEED patterns of Al_2O_3-supported clusters (Figure 2a and b) exhibit ring patterns which originate from grazing incidence electron-scattering processes in transmission through the clusters. The amorphous

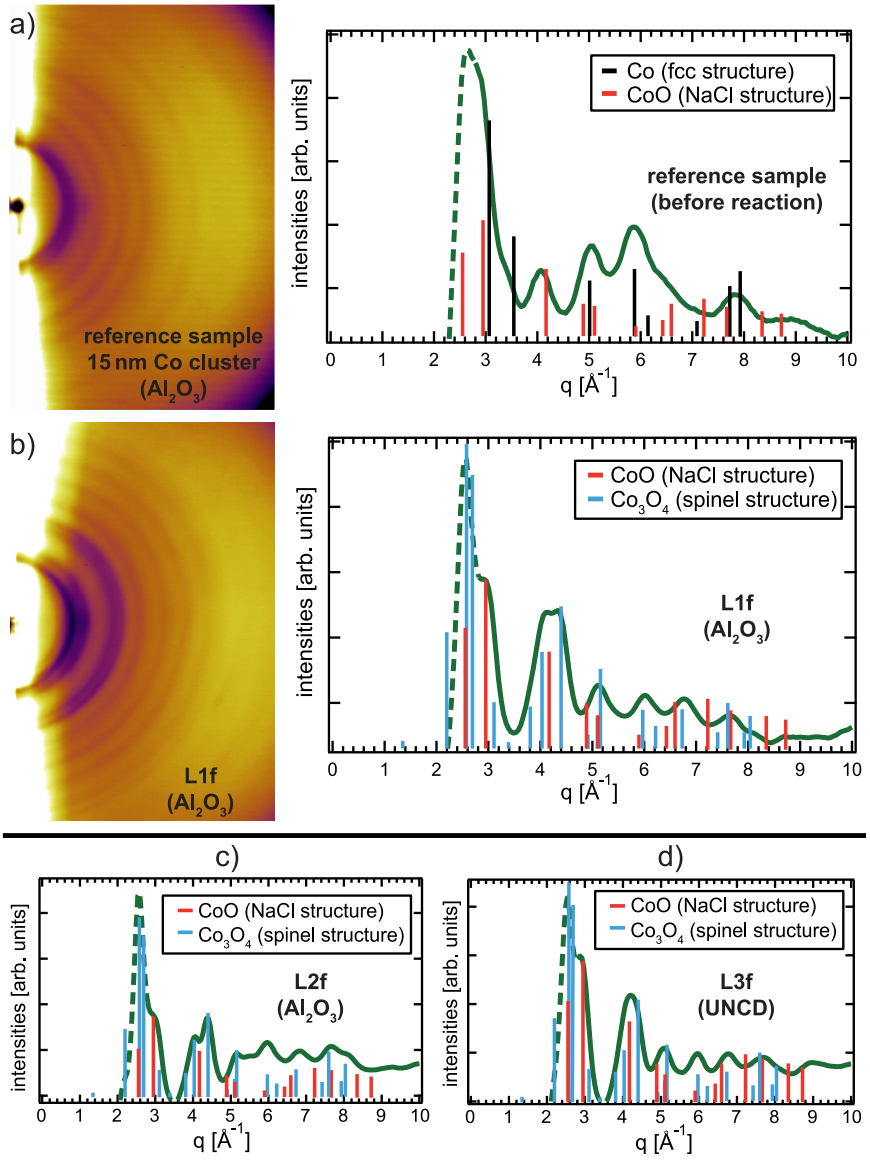

Figure 2. RHEED results from large clusters. RHEED images (left) are shown for a reference sample in (a) with cobalt clusters on Al_2O_3 before reaction and (b) sample L1f (d_i = 15 nm) after reaction exhibiting characteristic ring patterns. For better visibility, a smooth background is subtracted and high intensity is shown dark. The rings result in pronounced peaks in the angular averaged intensity curves (right). The first dashed peak at 2.5 $Å^{-1}$ contains artifact contributions from the electron gun. The colored vertical lines indicate the calculated positions and relative intensities for metallic Co (black), CoO (red), and Co_3O_4 (blue). (c, d) Profiles of larger clusters on Al_2O_3 (d_i = 22 nm, L2f) and UNCD (d_i = 21 nm, L3f), respectively, after reaction. Differences in the profiles originate from composition changes of the particles upon reaction.

substrate only contributes to a background signal and does not give rise to additional features.

No ring texturation is visible, showing that the clusters are randomly oriented on the sample surface which gives rise to Debye–Scherrer ring patterns analogously to conventional powder diffraction.[37,38] The radius of the diffraction rings corresponds to the length of the scattering vector q and thus is characteristic for the elemental molecular spaces. On the right side of the RHEED patterns the angular averaged intensity curves are plotted against the inverse lattice spacing showing the rings as pronounced peaks. A smooth background is subtracted for better visibility. Using conventional powder diffraction theory and bulklike crystallographic structures the expected positions and relative intensities of metallic Co (fcc structure; the bulk hcp phase only occurs for particles larger than 30 nm[39]), CoO (NaCl structure), and Co_3O_4 (spinel structure) are calculated with the software PowderCell 2.3.[40] This approach neglects the finite size of the particles used in this study. Nevertheless, the calculations can be used as a reference in order to identify strong peaks. The height of the first calculated peak in each graph is normalized to the corresponding experimental one. Before reaction (Figure 2a), the large clusters show contributions of only Co and CoO in

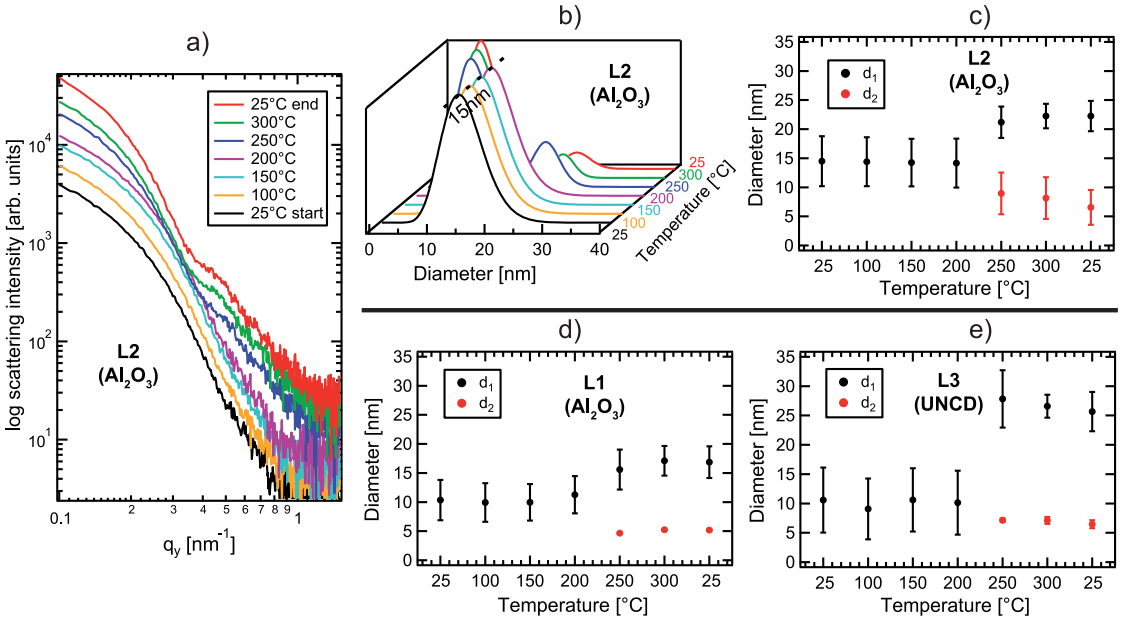

Figure 3. ***In situ*** **GISAXS results from large clusters under reactive conditions. (a) Horizontal cuts of the GISAXS images recorded between 25 and 300 °C of sample L2 (d_i = 22 nm, Al_2O_3). The spectra are offset vertically for clarity. The changes in spectra can be fitted by the horizontal size distributions shown in (b) where a splitting into two sizes at 250 °C gives the best results. (c) Identified diameters shown as a function of temperature for sample L2. (d, e) Qualitatively the same behavior is shown for clusters on L1 (d_i = 15 nm, Al_2O_3) and L3 (d_i = 21 nm, UNCD). On UNCD (e), the size changes are more prominent when compared to Al_2O_3. The error bars in (c−e) represent the width of the fitted size distributions.**

accordance with the GIXANES measurements. After the reaction, the RHEED pattern significantly changes, with a strong double peak at 4.2 $Å^{-1}$ from Co_3O_4 (Figure 2b). Additionally, contributions of CoO remain present. In comparison, Figure 2c (sample L2) shows a more pronounced double peak structure which can be attributed to a higher Co_3O_4 amount in the larger particles on Al_2O_3 after reaction.

The main difference of clusters deposited on UNCD (Figure 2d) is that the CoO contribution is higher compared to Al_2O_3 (L1f and L2f, Figure 2b and c); hence, the CoO peak at 3 $Å^{-1}$ is very pronounced and the peak structure around 4.2 $Å^{-1}$ is dominated by a single peak from CoO, which is located in between the double peak of Co_3O_4. The crystallographic cluster properties as obtained from RHEED for L1, L2, and L3 are in overall good agreement with the compositions found with GIXANES (Figure 1) at the end of the treatment, further supporting the identified structural transition.

In addition to the composition and structural changes detected by GIXANES and RHEED, the morphology of the particles during reaction is monitored by *in situ* GISAXS. In Figure 3a, the horizontal cuts of the GISAXS images for L2 point to a pronounced change in morphology at about 250 °C. The size distribution analysis using a peak-fitting routine within the Irena analysis package (see the Methods) reveals the change in lateral sizes of the clusters as a function of temperature (see Figure 3b). The initial sizes are smaller compared to TEM measurements, which might be a GISAXS artifact due to the subtracted background for the rough substrates used in this study (see the Methods). In contrast to TEM (see below), a large number of particles (>10^7) is probed by GISAXS, thus providing high statistical relevance of the observed particle properties.

For sample L2 (Figure 3b,c), the distribution starts with a single size at 25 °C and splits into two peaks at 250 °C where objects with both a larger and smaller lateral size compared to d_i are found. A similar development is observed for L1 (smaller clusters, see Figure 3d). Again, the appearance of two sizes at 250 °C can be observed. In contrast to the alumina-supported clusters (L1, L2), the size change is more distinct on UNCD (L3, see Figure 3e). For L1 and L3 in Figure 3d,e, the fit exhibits quite narrow error bars. The temperature-dependent evolution of the horizontal GISAXS cuts (see Figure 3a for L2 and Figure S2a/b, Supporting Information, for L1 and L3) and the deduced characteristics of the size distributions are similar for all three samples. For the precise origin of the size splitting, different scenarios are possible. The oxidized clusters may consist of smaller subunits detected by GISAXS.[41] Indeed, a grainy structure of the shells can be seen in TEM images (see below in Figure 6). Another explanation may be a core−shell structure with sizes corresponding to the outer and the inner diameter of the particles, respectively. In the literature, GISAXS studies of hollow structures are available using special form factors.[42,43] Since the bimodal distribution only evolves at higher temperatures,

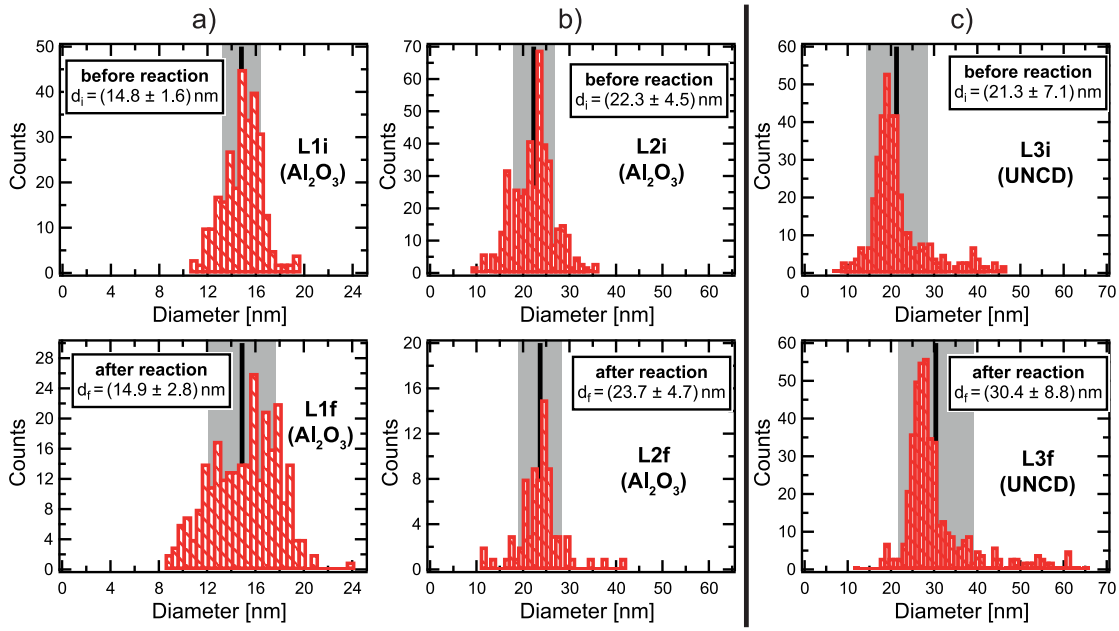

Figure 4. Distributions of lateral sizes for large clusters obtained from TEM images before (top) and after (bottom) reaction. The black line represents the mean size and the light gray area the standard deviation of the distribution. For L1i/f (a) and L2i/f (b) on Al_2O_3, only a small change in the mean size can be observed. (c) Particles on carbon (L3i/f) show a significant increase of lateral size by about 9 nm.

multiple sizes initially produced by the cluster source can be excluded as an origin. Thus, the second peak at larger sizes is representative for the outer morphology of the particles. In comparing Figure 3e to Figure 3c,d, the lateral size increase of the particles on UNCD appears much more pronounced compared to Al_2O_3. As we will show later, this observation is supported by TEM measurements. In all three cases, the size distribution splits at 250 °C where the clusters mainly consist of CoO (see Figure 1: L1—100% CoO; L2—65% CoO, 35% Co_3O_4; L3—100% CoO) and no metallic Co is present.

The combination of GIXANES, RHEED, and GISAXS reveals a change in stoichiometry, structure, and size depending on the initial diameter of the particles and on the substrate. In order to gain deeper insight into the geometric properties we now use high resolution TEM measurements that were performed before and after reaction. Co clusters on TEM grids are deposited simultaneously with the samples used for GIXANES, GISAXS, and RHEED. TEM grids covered by a thin layer of Al_2O_3 are used for comparison to Al_2O_3 samples (see the Methods). In place of UNCD samples, amorphous carbon grids serve as corresponding TEM supports. From overview images, we extract the size distributions assuming a spherical shape of the particles; see Figure 4a,b for large clusters on Al_2O_3 (L1, d_i = 15 nm and L2, d_i = 22 nm). Only minor size changes can be observed after the reaction. The relatively broad distributions originate from the particular parameters used for the cluster source in order to achieve the high deposition rates needed for these experiments. On carbon (L3, d_i = 21 nm), a significant increase of about 9 nm is seen (Figure 4c), similar to the GISAXS results (compare parts c—e of Figure 3).

A closer look at representative high-resolution TEM images (bright field) before reaction is shown in Figure 5 for selected clusters. The particle on Al_2O_3 in Figure 5a consists of a darker core and a brighter shell. The latter is caused by partial oxidation at the surface due to exposure to air after deposition. In Figure 5b, different atomic structures in the core and shell region can be observed, respectively, supporting the RHEED findings (see Figure 2). On amorphous carbon, a variety of different shapes is observed for large clusters (see Figure S3, Supporting Information), such as spheres, triangles, and rectangles (Figure 5c). These nonspherical shapes on carbon might be a reason that the sizes obtained from GISAXS are consistently smaller than those obtained in the TEM (compare Figure 3 and 4). Again, the core exhibits an atomic structure different from that of the oxide shell.

Upon reaction, the particles are strongly modified, see Figure 6, showing representative bright field TEM images from samples L1, L2 (on Al_2O_3), and L3 (on carbon). In all three cases, the core appears bright and is surrounded by a darker area. The outermost region again is brighter. The images hint at hollow nanoparticles of different sizes originating from the nanoscale Kirkendall effect, which is well-known for several materials like Co, Al, and Fe.[18—20,25] In brief, this effect is based on the different diffusion rates of metal ions (fast) and oxygen ions (slow)[22—24] in conjunction with a radial concentration gradient. This leads to

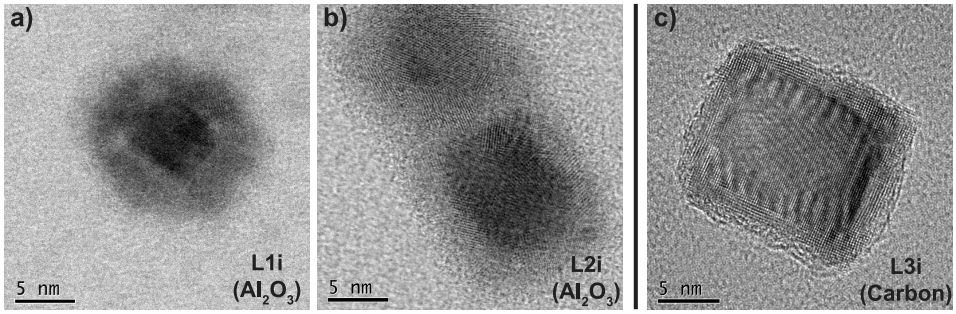

Figure 5. Representative TEM images of large clusters on (a, b) Al_2O_3 (L1i, d_i = 15 nm; L2i, d_i = 22 nm) and (c) carbon (L3i, d_i = 21 nm) before reaction. All particles show brighter shells compared to the core indicating a partial oxidation at the surface. In (c), a pronounced structural difference from the rectangular Co core of about 9.5 × 12.4 nm^2 to the shell region (cobalt oxides) is evident.

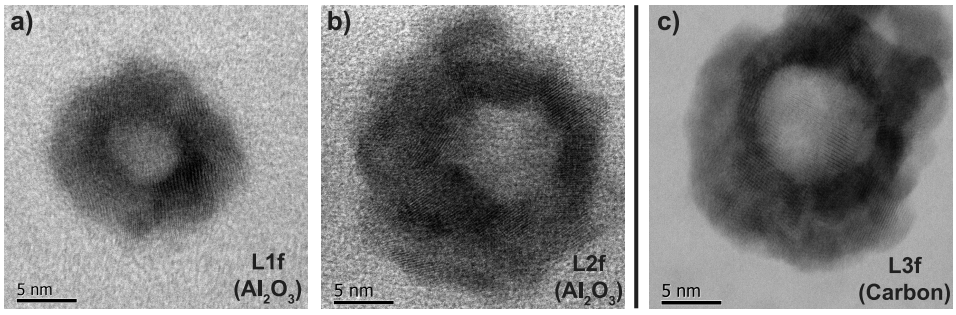

Figure 6. Representative TEM images of large clusters on (a, b) Al_2O_3 (L1f, d_i = 15 nm; L2f, d_i = 22 nm) and (c) carbon (L3f, d_i = 21 nm) after the TPRx experiment. In all three cases, the core appears bright, surrounded by a darker area. The outermost region again shows up brighter. The images indicate hollow particles that are a typical result of the Kirkendall effect. On carbon (c), a bright disklike structure around the shell is visible.

the formation of hollow particles, in our case consisting of a shell of cobalt oxides as seen in GIXANES and RHEED (see Figure 1 and 2).

Whereas in Figure 6a the particle is of approximately spherical shape and has an inner oxide shell diameter of about 5 nm, the morphology of (b) and (c) consists of several crystallographic domains. The inner diameter in (b) and (c) is about 7 and 8 nm, respectively. Particularly in (c), the shell is surrounded by a large bright area. This hints to a disklike geometry with a lower height formed around the particle during oxidation; see also Figure S4 (Supporting Information) and the Discussion section. The size changes observed exemplarily by TEM confirm the statistically more relevant GISAXS results (see Figure 3).

Medium-Sized Clusters. Dark-field TEM images of particles in the intermediate size range on Al_2O_3 (M1, d_i = 4.4 nm) are shown in Figure 7. The histogram of particle size before reaction is shown below the TEM image in Figure 7a. After the reaction (Figure 7b), no significant changes in the TEM image can be observed, indicating that these particles are particularly stable. GISAXS measurements taken on a comparable sample to M1 (Al_2O_3 support, same deposition conditions) are shown in Figure S5 (Supporting Information) and confirm the TEM findings.

Like in the case of large particles, GIXANES is again applied to determine the chemical composition during the treatment; see Figure 8. The clusters of sample M1 (on Al_2O_3) are already oxidized after air exposure at room temperature and consist of about 90% CoO. During the reaction experiment, only a small fraction of the initial CoO is converted to Co_3O_4, so in the final stage the particles consist of about 75% CoO and 25% Co_3O_4. The averaged valence remains at about 2.2 and confirms the robustness of the oxidation state of these medium-size clusters on Al_2O_3 during the treatment. In the case of UNCD-supported particles (M2), the qualitative behavior is quite similar, see Figure S6 (Supporting Information). The initial CoO content (60%) is lower compared to the Al_2O_3 supported particles and leads to a final composition of about 50% CoO and 50% Co_3O_4. Again, the averaged valence remains almost constant at about 2.3. In both cases, it is smaller compared to larger clusters on the same substrate (cf. Figure 1).

Small Clusters. To extend the size range to smaller particles, clusters are formed and deposited with the laser vaporization source described in the Methods. The typical particle size is 2 nm for samples S1 and S2; see the Supporting Information for a size histogram of particles in the cluster beam (Figure S8). STEM HAADF measurements were performed for Al_2O_3 and amorphous carbon supported clusters (S1, S2); see Figure 9. Although some compact clusters can still be observed (arrow "I"), in many cases, the particles on Al_2O_3

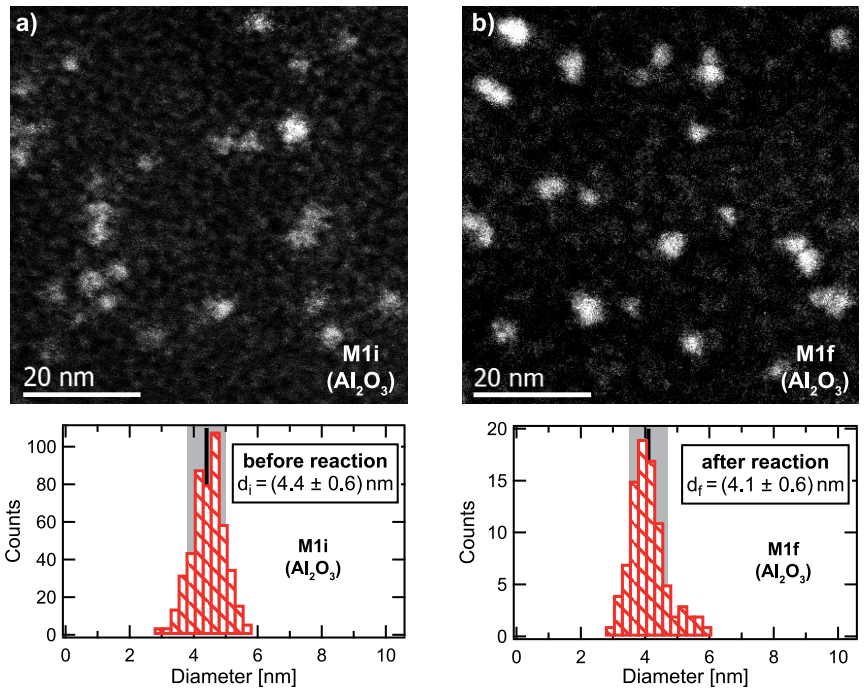

Figure 7. STEM HAADF study of intermediate clusters deposited on Al_2O_3 (d_i = 4.4 nm, M1). The black line represents the mean size and the light gray area the standard deviation of the distribution. No significant changes before (a) and after (b) the TPRx experiments are visible.

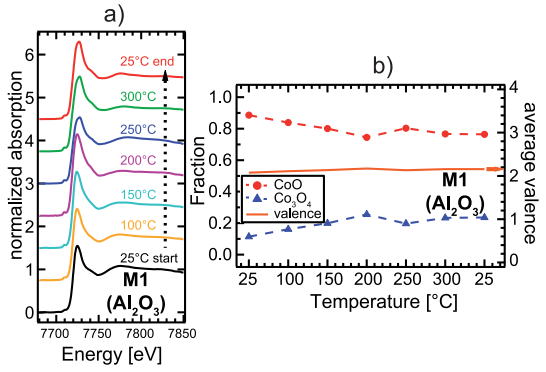

Figure 8. (a) Normalized GIXANES spectra of intermediate clusters on Al_2O_3 (d_i = 4.4 nm, M1) at different temperatures under reactive conditions. The spectra are offset vertically for clarity. (b) Composition of clusters as obtained from GIXANES (cf. Figure 1). Only CoO (red circles) and Co_3O_4 (blue triangles) are present; no elemental Co can be detected. The averaged valence (solid curve) shows no significant changes.

(Figure 9a) are surrounded by single atoms or smaller aggregates (bright spots, arrows "II"). This hints at a restructuring or partial fragmentation even at air and room temperature. On amorphous carbon, mainly crystalline compact clusters can be observed also after air exposure (Figure 9b). Single atoms or smaller aggregates are present to a lesser extent compared to Al_2O_3 (see the Supporting Information for overview images, Figure S9). This indicates that the restructuring/fragmentation process is assisted by the presence of Al_2O_3 or by edges of Al_2O_3 islands often produced by the atomic layer deposition (ALD) process on inert surfaces.[44−46]

Figure 10 shows the compositional evolution of Al_2O_3-supported 2 nm clusters. Like in the case of intermediate sizes, the particles are already oxidized after air exposure and consist of about 80% CoO and 20% Co_3O_4 before the reaction experiment. For these small clusters, GIXANES does not primarily probe the structural properties but rather the oxidation state (average valence), which also reflects chemical bonding to the substrate. During the treatment, only small changes are visible leading to an almost constant averaged valence of about 2.2 and indicating the robustness of the oxidation state of these particles. In the final stage, the particles consist of about 70% CoO and 30% Co_3O_4. The *in situ* GISAXS measurements for clusters on sample S1 are shown in Figure S10 (Supporting Information) and display no morphological changes or sintering under reactive conditions.

For even smaller clusters (d_i = 1.4 nm), the qualitative evolution of the oxidation state is quite similar. The GIXANES spectra in Figure S12 (Supporting Information) again display an averaged valence of about 2.15, which shows no significant changes during the treatment. The final composition is determined to 80% CoO and 20% Co_3O_4 indicating a very robust CoO phase even for the smallest particles investigated here.

DISCUSSION

The most diverse morphological and compositional behavior is observed for the large particles with a

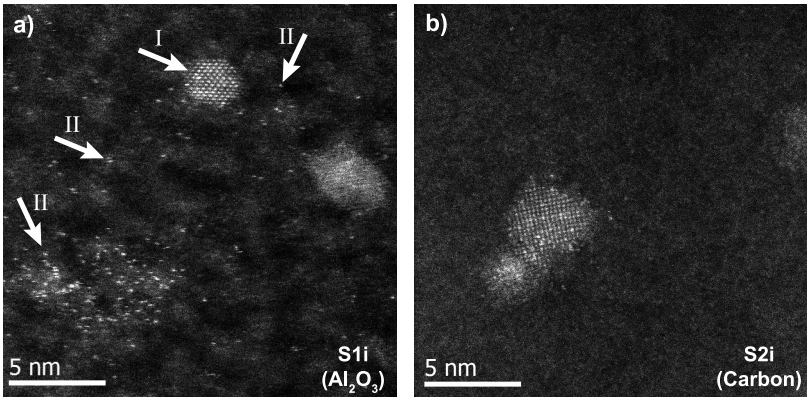

Figure 9. Representative STEM HAADF images of small clusters deposited on Al_2O_3 (a) and carbon (b). The bright dots on the TEM images originate from Co atoms or extremely small Co clusters (exemplarily marked by arrows "II"). On Al_2O_3 (a), more of these restructured/fragmented systems are found compared to carbon support (b).

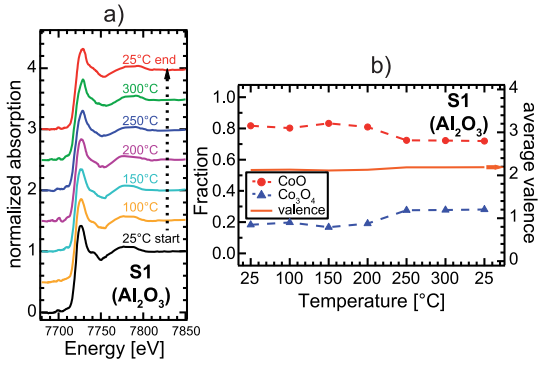

Figure 10. Evolution of the oxidation state of small clusters. (a) Normalized GIXANES spectra on Al_2O_3 (d_i = 2 nm, S1) at different temperatures under reactive conditions. The spectra are offset vertically for clarity. (b) Composition of clusters as obtained from GIXANES (cf. Figure 1). Only CoO (red circles) and Co_3O_4 (blue triangles) are present, no elemental Co can be detected. The averaged valence (solid curve) shows no significant changes.

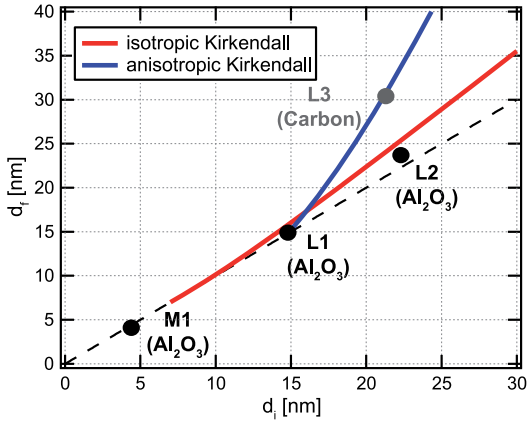

Figure 11. Change of lateral cluster diameter upon reaction. Measured data points obtained from the TEM histograms (see Figure 4) are shown as circles. The expected size changes due to the Kirkendall effect are based on simple geometric models. For the isotropic Kirkendall effect (red curve), the diffusing material is assumed to form a spherical shell around the initial oxide shell. In the case of the anisotropic Kirkendall effect where a disk is formed around the cluster at the interface to the substrate (blue curve) the size changes are more pronounced. The dashed black line illustrates the case of no size change during reaction and serves as a guide to the eye.

diameter of the order of 20 nm. They show a pronounced Kirkendall effect and significantly different properties depending on the substrate. Figure 11 summarizes the size changes observed by TEM by relating the average diameters before reaction (abscissa) to those after the reaction (ordinate) for different substrates (black *versus* gray circles). The particles on Al_2O_3 (L1 and L2, black) only undergo small size changes compared to UNCD/carbon supported species (L3, gray). An explanation can be found by applying a simple geometric model: given that the Co content of each cluster remains unchanged during reaction the expected outer diameter can be estimated. For the inner diameter of the hollow spheres we assume that it corresponds to the initial size of the metallic Co core, and we neglect slow inward diffusion of oxygen.[27] Then, the final outer diameter d_f can be expressed as

$$d_f^3 = d_i^3 + \frac{\rho_{Co}}{\rho_{Co_3O_4}} (d_i - 2w_S)^3 \qquad (1)$$

where d_i is the diameter of the Co-CoO core−shell nanoparticles before reaction, ρ_{Co} and $\rho_{Co_3O_4}$ are the densities of the metallic Co and its oxide, respectively, and w_S the thickness of the oxide shell which is measured to be 3.5 nm. Note that compared to metallic cobalt (ρ_{Co} = 8.80 g/cm^3) the densities for the two oxides (ρ_{CoO} = 6.45 g/cm^3; $\rho_{Co_3O_4}$ = 6.07 g/cm^3) observed here are quite similar; hence, we only used the density of Co_3O_4 to describe the final state of the oxidation although there is still some CoO present.

In the case of an isotropic Kirkendall effect (*i.e.*, Co diffusion is not affected by the substrate), d_f follows the red curve in Figure 11. Starting from 7 nm where the entire volume of the clusters is already oxidized after air exposure, the expected size change becomes larger with increasing initial particle size. For larger

clusters, the initial amount of material that is not oxidized at the beginning and can diffuse through the oxide shell is much larger and leads to a more pronounced size change.

Smaller cobalt clusters below 7 nm do not undergo a Kirkendall transition as displayed in Figure 7 (M1, d_i = 4.4 nm), in agreement with observations for chemically prepared Co particles (6 nm) reported in literature.[47] This is not surprising given the general observation that the oxidation process of metals can be described by a rapid initial reaction, passivating the remaining metallic material such that subsequent reactions are extremely slow.[48,49] This leads to stable 2−10 nm thick oxide films in bulk materials.[49,50] For nanoscale objects a few nanometers in diameter, this means that the entire volume of particles oxidizes upon air exposure and no further oxidation or size change occurs during the catalytic reaction.

The experimental data for the Al_2O_3-supported particles (L1, L2) are in reasonable agreement with the model curve (Figure 11). On amorphous carbon (L3), however, the measured lateral size after reaction is significantly larger than predicted by our model which is already seen in the GISAXS (Figure 3) and TEM histogram (Figure 4) data. In fact, this points to a substantial morphology difference because the evolution of the total particle volume is expected to be similar on both substrates. TEM images (Figure 6c and Figure S4, Supporting Information) suggest that the particles are surrounded by a plateau that appears to be of lower height than the cluster itself. In order to model this behavior, we introduce an anisotropic form of the Kirkendall effect, where the diffusion is affected by the substrate. Within this model, the Co atoms do not diffuse uniformly in all directions but accumulate on the substrate around the particle. The result is a flat disk around the particles that is modeled by a cylindrical volume. The expected outer diameter of the particle is then expressed by that of the disk and plotted in Figure 11 (blue curve). The thickness of the disk (3.5 nm) is chosen to match the experimental data point obtained from TEM histograms (see Figure 4c). Further verification of the anisotropic Kirkendall effect would require more data points toward larger clusters which are not easily produced with the particle sources available here. Nevertheless this analysis shows that the morphologic changes induced by the Kirkendall effect differ qualitatively for Co clusters of similar size but different substrates. This observation could be explained by the following microscopic mechanisms: first the outward diffusion of cobalt is essentially terminated when the cobalt is oxidized and incorporated in the cobalt oxide lattice at the particle surface. When a diffusing cobalt atom approaches the substrate interface on carbon it continues to diffuse laterally until the rim of the particle is reached where it can be oxidized in the gas environment. This results in an accumulation of cobalt oxide close to the particle substrate interface, eventually creating the observed disklike features. In contrary, on Al_2O_3 oxidation might occur directly at the interface, immediately terminating the diffusion. In a sense the Al_2O_3 substrate provides a more isotropic chemical environment in terms of oxygen presence compared to carbon surfaces. A second possibility is the significantly larger diffusivity of cobalt and cobalt oxide on carbon as compared to Al_2O_3 (see, *e.g.*, refs 51 and 52). This enables a more pronounced cobalt spread out around the particles at carbon substrates.

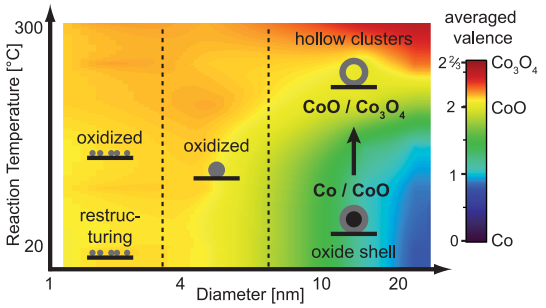

Figure 12. Schematic summary of observed morphological and compositional processes of Co clusters deposited on Al_2O_3 as a function of temperature and cluster size. The color-coded averaged valence is interpolated on the basis of the GIXANES measurements (see Figures 1, 8, and 10) and represents the composition of the particles. For the largest clusters which exhibit an oxide shell before reaction, hollow particles are formed during the reaction. The transformation of the initial Co/CoO to the final CoO/Co_3O_4 mixture is indicated in the plot and can be followed by the color code. At cluster sizes considerable less than 7 nm but more than 1.4 nm the particles do not contain metallic cobalt already prior to the TPRx experiments. The smallest clusters (<4 nm) tend to partial fragmentation/restructuring on the Al_2O_3 substrate upon air exposure, even at room temperature, but show no further changes upon heating under reactive conditions.

In the following discussion, we summarize the size-dependence of morphological and compositional changes upon the reaction for the case of Co clusters on Al_2O_3. A schematic overview of the observed processes is shown in Figure 12. During the treatment, an overall sintering resistance could be observed for all sizes. Small particles in the size range of about 2 nm tend to become partially restructured in air by forming smaller aggregates or single atoms at least on Al_2O_3-covered TEM grids. During the reaction experiments, only slight compositional changes can be observed, indicating a strongly CoO dominated stable oxidation state of these particle sizes. A similar robust CoO phase is reported for size-selected subnanometer cobalt clusters under oxidative dehydrogenation reaction conditions for cyclohexene[9,33,34] and cyclohexane.[53] Clusters in the size range of 4−7 nm maintain a compact shape and are fully oxidized (no metallic cobalt) after air exposure at room temperature as well.

During the TPRx experiment they show only minor changes in their composition and shape resulting in a slightly lower CoO content compared to the smallest particles. Larger clusters up to sizes of 25 nm show a core−shell structure with a metallic cobalt core and a CoO shell. During the oxidative dehydrogenation of cyclohexane the metallic cobalt is converted into cobalt oxides (CoO and Co_3O_4) which results in hollow particles that are formed due to the Kirkendall effect, consisting of CoO and Co_3O_4. The fact that the most pronounced morphologic changes coincide with the maximum CoO content (compare Figure 3 and Figure 1) at 200−250 °C shows that during further conversion to Co_3O_4 the particles essentially retain their shape. This is consistent with observation of chemically prepared Co particles on glass.[23] In general smaller clusters mainly consist of CoO whereas for larger particles Co_3O_4 is more prominent after the treatment. Therewith a direct correlation between morphological and compositional changes can be deduced for large particles.

Although not systematically studied, we do not expect significantly altered particle properties due to the presence of cyclohexane, for two reasons: (1) The catalytic reaction most likely occurs by hydrogen abstraction over oxide sites on the particle.[12] Hence the predominant role of oxygen gas is to create suitable reaction sites by oxidizing the clusters. Since the amount of oxygen is much higher compared to cyclohexane, possible reduction effects by cyclohexane are overwhelmed by oxidation processes at the particle surface. (2) In pure oxygen, a similar morphological behavior (including the Kirkendall effect) is reported in the literature for the reaction path (Co → CoO → Co_3O_4) of chemically prepared nanoparticles.[27,47]

The formation of hollow spherical shapes via the nanoscale Kirkendall effect is well documented for particles prepared in solution,[18,26] by wet chemical methods with subsequent deposition on flat and porous supports,[23,27,47,54,55] and at liquid−gas interfaces.[28] Here, we demonstrate that the same mechanism also is at work for physically produced and soft-landed clusters subsequently exposed to gaseous environments with critical particle sizes for the onset of the Kirkendall effect[47] similar to chemical preparations. We find a significant influence of particle-surface interaction by comparing two different substrates which is in line with reports on a broad temperature range of the Kirkendall transition depending on environment (see, *e.g.*, refs 23 and 28) and capping.[56] Since the same mechanism has been also found for a whole range of materials[18−21] we expect that our results can be generalized to systems beyond Co as well.

Whereas the Kirkendall mechanism as such seems to be rather universal, irrespective from the specific environment, we observe significant differences in the morphological behavior for large clusters depending on the substrate. While for Al_2O_3 an isotropic Kirkendall effect is found, particles on UNCD change their morphology and form a flat disklike area around the initial particle with a hollow core. Such an anisotropic Kirkendall effect results in a dramatically changed horizontal diameter observed by TEM and GISAXS (see Figure 3e and 4c). Since the surface to volume ratio is an important parameter for catalysis this may have a significant effect on the reaction kinetics. In fact, the particle surface in the case of the isotropic Kirkendall effect on Al_2O_3 increases only by ∼20% compared to the initial compact clusters (22 nm diameter), whereas on UNCD the increase is in excess of 40%. Studies aiming at the quantification of catalytic efficiency need to take into account these morphological variations, which significantly affect the number of available reaction sites at the particles' interfaces.

CONCLUSIONS

Gas-phase produced Co nanoparticles in a broad size range from 1.4 nm to beyond 20 nm are soft landed on two different substrates, *i.e.*, Al_2O_3 and UNCD. During the oxidative dehydrogenation of cyclohexane, structural, stoichiometric, and morphologic changes of the cobalt clusters are observed by a combination of various techniques. Due to transport in air, small- and intermediate-sized particles (<7 nm diameter) are mainly oxidized to CoO while large clusters (>10 nm) are only partially oxidized and consist of a metallic Co core and a CoO shell. Our studies reveal that for large particles Al_2O_3 supports the formation of Co_3O_4, whereas on UNCD the transformation of metallic cobalt into its oxides starts at higher temperatures, resulting in a lower Co_3O_4 content using the same temperature treatment. The Al_2O_3-supported particles show an isotropic Kirkendall effect, similar to that frequently reported in the literature for particles produced by wet-chemical methods. On UNCD or amorphous carbon, a dramatic lateral size change is found which we attribute to an anisotropic form of the Kirkendall effect where a flat disklike structure around the particles is observed. During reaction the intermediate (4 to 5 nm) and small clusters (2 nm) show no significant changes in composition and morphology revealing a robust CoO phase for these sizes.

Our study opens the route toward a controlled and precise adjustment of the stoichiometry of gas-phase prepared Co nanoparticles from CoO to Co_3O_4 and in between by simply preselecting the size of the produced particles or by varying pretreatment or reaction conditions (see Figure 12), thus providing a handle to systematically control efficiency and selectivity of catalytic reactions. In fact CoO nanocrystals have been shown to act as efficient

photocatalysts for solar water splitting,[11] while Co_3O_4 is a promising catalyst for the oxidation of CO[57,58] and the dehydrogenation of cyclohexane,[9,12] to name a few examples.

METHODS

To investigate the support effects two different substrate materials are used for cluster deposition, namely ultrananocrystalline diamond (UNCD) and alumina. For *in situ* GIXANES, GISAXS, and TPRx studies, UNCD and alumina-coated silicon wafer chips with a size of 10 × 10 mm^2 are used for cluster deposition. The UNCD-coated silicon wafers (UNCD, 25 Aqua DoSi, Advanced Diamond Technologies) consist of a 300 nm thick UNCD film on top of a doped silicon wafer and have a surface root-mean-square (RMS) roughness of ~10 nm estimated from AFM images.[36,59] Alumina supports are prepared by atomic layer deposition[60] (ALD) with approximately three monolayers (ML) on top of the naturally oxidized doped silicon wafer, yielding an amorphous surface with RMS roughness of ~0.7 nm estimated from STM images.[61] For *ex situ* TEM investigation, the alumina layers are coated with the same procedure on carbon covered TEM grids. The alumina coated Si chips and TEM grids are used for cluster deposition under the same conditions and resulting samples on Si chips and TEM grids are treated together in the same reactor during exposure to the reaction gas.

For the production of a large size range of Co clusters, we employ both an arc cluster ion source (ACIS) for large clusters[62] and a laser vaporization source[63] for smaller species. After beam formation and differential pumping, the clusters are deposited onto TEM grids mounted next to the substrate at the same time. Coverages well below one monolayer of clusters are chosen to ensure well-separated particles. No significant sintering or aggregation is detected upon subsequent chemical treatment, which we attribute to the large cluster surface interaction of this system.[35]

Inside the ACIS, an arc is ignited in a hollow Co cathode, resulting in metal−vapor plasma in the high temperature area. An inert gas atmosphere composed of helium and argon is used as a buffer gas to enable cluster aggregation. The gas flux is optimized for a high cluster yield for the respective cluster sizes needed, resulting in a flux ratio of Ar and He in the range F_{He}/F_{Ar} = 0−0.4. The total pressure within the cathode is in the order of 30 mbar. The charged clusters are size selected by an electrostatic quadrupole. The substrates (Al_2O_3, UNCD) and corresponding TEM grids (Al_2O_3, carbon) are positioned directly behind the quadrupole to obtain sufficient sample coverage needed for these experiments. The deposition takes place at a pressure of 10^{-7} mbar to 10^{-6} mbar. An average coverage of about 500−1000 particles per μm^2 has been reached. As a side effect of the short distance between the quadrupole exit slit and the sample a slightly widened size distribution is expected compared to previous depositions performed with this setup.[61,62] For cluster sizes used in this work the kinetic energy per atom remains below 20 meV which is estimated based on a spherical cluster shape with measured cluster diameters. These energies are well within the regime of soft-landing conditions observed experimentally[64,65] and obtained from simulations.[66,67] Nevertheless, the impact and the interaction with the substrate may result in slightly oblate cluster shapes.[68,69] Occasionally, multiple particles of different sizes are observed, which hints to agglomeration of particles in the gas phase[70,71] (see, *e.g.*, Figure S3, Supporting Information).

The laser vaporization source is implemented in an UHV cluster deposition setup.[72] The source uses two pulsed Nd:YAG lasers (wavelength = 532 nm, repetition rate = 10 Hz) to ablate material from a high purity Co target. As the lasers are triggered, a synchronized pulse of helium gas enters the source chamber to cool down the plume of material created at the surface of the target and cluster nucleation starts. This mixture of gas, atoms, and clusters expands into the vacuum through a conical nozzle after which cluster growth stops. By extraction and differential pumping, a well-collimated cluster beam is formed. The Co clusters have a size distribution centered at a diameter of about 2 and 1.4 nm with a full width at half-maximum of 0.7 and 0.6 nm, respectively (see Figures S8 and S11, Supporting Information). The clusters are deposited in a low energy regime (well below 1 eV/atom). This ensures soft landing, thus minimizing the cluster deformation and the damage of the substrate. The base and working pressures in the deposition chamber are 1 × 10^{-9} and 2 × 10^{-7} mbar, respectively. These vacuum conditions minimize contamination of the deposited clusters.

After the deposition process, the samples are exposed to air for transfer to the AFM and TEM for determination of vertical and lateral cluster diameter, respectively, as well as the deposited coverage. Subsequent X-ray scattering and absorption studies have been conducted at the Advanced Photon Source at Argonne National Laboratory. The final particle structure and composition after the reaction is determined by *ex situ* RHEED and TEM. Between the different stages a time of weeks to months elapsed.

For TEM measurements, an aberration-corrected JEM ARM200F (JEOL, Corrector: CEOS) operated at 200 keV is used. The microscope is equipped with a JED 2300 (JEOL) energy-dispersive X-ray-spectrometer (EDXS) for chemical analysis. Aberration corrected STEM (scanning transmission electron microscopy) imaging in high-angle annular dark field (HAADF) and annular bright field (ABF) modes is performed under the following conditions. HAADF and ABF both were done with a spot size of approximately 0.13 nm, a convergence angle of 30−36° and collection of semiangles for HAADF and ABF of 90−170 mrad and 11−45 mrad, respectively.

GISAXS/GIXANES/TPRx. After cluster deposition, samples are studied using a unique system combining TPRx with *in situ* GISAXS and GIXANES developed at the 12-ID-C beamline of the Advanced Photon Source at Argonne National Laboratory.[33] A detailed description of the experimental setup and data analysis can be found in previous reports.[12,34,73,74] In brief, the samples, both on chips and TEM grids, are positioned on a ceramic heater (Momentive Performance Materials, Inc.) in a home-built continuous flow reaction cell designed for TPRx.[34] The reactor is mounted on a computer-controlled goniometer and equipped with Kapton windows to facilitate X-ray transmission. Prior to the combined *in situ* TPRx, GIXANES, and GISAXS experiments, the reaction cell is purged with cycles of pumping and flushes of pure helium gas. Then the reactant gas mixture of cyclohexane (4000 ppm in He) and ultrapure oxygen (99.9999%) is introduced. During the TPRx studies, a mixture of cyclohexane and O_2 (30 and 1.2 sccm rates, respectively) flows continuously into the cell, resulting in a cyclohexane to oxygen ratio of 1:10, respectively. A gas-mixing unit consisting of calibrated mass flow controllers (Brooks Model SLA5850) combines the gases and controls the rate of flow into the reaction cell. Additionally, the pressure within the cell is held constant at 1070 mbar. The sample temperature is calibrated and measured by a K-type thermocouple attached to the heater side. The actual deviation from the programmed temperature profile is found less than 1 °C during the whole experiment. After 20 min at 25 °C, the sample is ramped to 100 °C, then ramped in steps of 50 °C up to 300 °C; finally, the sample is cooled to room temperature. Both the ramping and cooling temperature rates are kept at 10 K/min, and during GISAXS and GIXANES data acquisition the temperature is held constant for 15 min at each step. Reaction products were not analyzed due to insufficient signals resulting from low cluster coverage. The GISAXS experiments are performed to monitor changes in cluster size and shape during TPRx using X-rays of 8 keV energy. The sample is slightly tilted toward the incoming beam so X-rays are scattered off the sample surface near the critical angle (0.15°) of the substrate. The 2D GISAXS images are recorded at each temperature step

with a 1024 × 1024 pixel CCD detector (MarCCD). Processing is done by taking an average of three close cuts in the q_y direction for horizontal information. To eliminate the influence of surface roughness from the substrate, subtraction of GISAXS cuts from alumina and UNCD blanks are performed on the sample data before analysis. The size distribution with spheroid form factor and Schulz−Zimm-type distribution is fitted using the Irena SAS data analysis package.[75,76] GIXANES data are collected at each temperature step, using a four-element fluorescence detector (Vortex 4 element SSD) mounted perpendicular to the X-ray beam and photon energies scanned between 7.55 and 7.85 keV. Reference spectra and energy calibration are obtained from Co standards (cobalt oxides in powder form and cobalt foil; Sigma-Aldrich) that are compressed and sealed between two layers of Kapton foil (except cobalt foil). The linear combination fitting of GIXANES data is processed with the IFEFFIT interactive software package with ATHENA and ARTEMIS graphical interfaces.[77]

RHEED. RHEED investigations are performed in a UHV system using 25 keV electron energy at incidence angles in a range of 0.5−1° to the surface. A CCD camera records the diffraction patterns appearing on a phosphor screen. For a more precise analysis, 200 single RHEED images are acquired and averaged, which results in a greatly improved signal-to-noise ratio. A well-defined diffraction pattern of nanoparticles on surfaces is obtained even with highly diluted systems (∼10 particles per μm^2).[37,38,78] The well-known Si(111)7 × 7 surface[79] serves as a reference to calculate atomic distances in the RHEED image.

Conflict of Interest: The authors declare no competing financial interest.

Acknowledgment. S.B., H.H., K.O., I.B., V.v.O., and K.-H.M.-B. acknowledge funding by the federal state Mecklenburg-Vorpommern within the project Nano4Hydrogen, the Federal Ministry of Education and Research (BMBF) within the project Light2Hydrogen, and the Deutsche Forschungsgemeinschaft (DFG) through the SFB652 (deposition of 4−22 nm size cobalt nanoparticles, RHEED, AFM and TEM characterization, and analysis and interpretation of RHEED and TEM data). S.B. acknowledges funding by the European Social Fund (ESF). K.H. and P.L. acknowledge support by the Research Foundation-Flanders (FWO, Belgium) and the Flemish Concerted Action (BOF KU Leuven, Project No. GOA/14/007) (deposition of 1.4 and 2 nm size cobalt clusters, characterization of the size distribution, AFM). The work at Argonne National Laboratory (*in situ* X-ray characterization, analysis of GISAXS and GIXANES data, and their interpretation) was supported by the U.S. Department of Energy (DOE), Office of Science, Basic Energy Sciences, Materials Sciences and Engineering Division, under Contract No. DE-AC-02-06CH11357. The *in situ* GISAXS/GIXANES experiments were carried out at the 12-ID-C beamline of the Advanced Photon Source of Argonne National Laboratory. The use of the Advanced Photon Source, an Office of Science User Facility operated for the U.S. Department of Energy (DOE), Office of Science by Argonne National Laboratory was supported by the U.S. Department of Energy (DOE) Office of Science, under contract No. DE-AC-02-06CH11357. We thank Dr. Michael Pellin (ANL) for coating the Si chips and TEM grids with ALD alumina.

Supporting Information Available: Additional GIXANES spectra, GISAXS cuts, TEM images, and size distribution of small Co clusters. The Supporting Information is available free of charge on the ACS Publications website at DOI: 10.1021/acsnano.5b00791.

REFERENCES AND NOTES

1. Hashmi, A. S. K.; Hutchings, G. J. Gold Catalysis. *Angew. Chem., Int. Ed.* **2006**, *45*, 7896–7936.
2. Bullock, R. M. Abundant Metals Give Precious Hydrogenation Performance. *Science* **2013**, *342*, 1054–1055.
3. Cuenya, B. R. Synthesis and Catalytic Properties of Metal Nanoparticles: Size, Shape, Support, Composition, and Oxidation State Effects. *Thin Solid Films* **2010**, *518*, 3127–3150.
4. Mazzacano, T. J.; Mankad, N. P. Base Metal Catalysts for Photochemical C-H Borylation That Utilize Metal-Metal Cooperativity. *J. Am. Chem. Soc.* **2013**, *135*, 17258–17261.
5. Kaden, W. E.; Kunkel, W. A.; Kane, M. D.; Roberts, F. S.; Anderson, S. L. Size-Dependent Oxygen Activation Efficiency over $Pd_n/TiO_2(110)$ for the CO Oxidation Reaction. *J. Am. Chem. Soc.* **2010**, *132*, 13097–13099.
6. Dry, M. E. Practical and Theoretical Aspects of the Catalytic Fischer−Tropsch Process. *Appl. Catal., A* **1996**, *138*, 319–344.
7. van der Laan, G. P.; Beenackers, A. A. C. M. Kinetics and Selectivity of the Fischer−Tropsch Synthesis: A Literature Review. *Catal. Rev.* **1999**, *41*, 255–318.
8. van de Loosdrecht, J.; Botes, F. G.; Ciobica, I. M.; Ferreira, A.; Gibson, P.; Moodley, D. J.; Saib, A. M.; Visagie, J. L.; Weststrate, C. J.; Niemantsverdriet, J. W. *Comprehensive Inorganic Chemistry II*; Elsevier: New York, 2013; pp 525−557.
9. Lee, S.; DiVece, M.; Lee, B.; Seifert, S.; Winans, R. E.; Vajda, S. Support-Dependent Performance of Size-Selected Sub-nanometer Cobalt Cluster-Based Catalysts in the Dehydrogenation of Cyclohexene. *ChemCatChem.* **2012**, *4*, 1632–1637.
10. Frenkel, A. I.; Cason, M. W.; Elsen, A.; Jung, U.; Small, M. W.; Nuzzo, R. G.; Vila, F. D.; Rehr, J. J.; Stach, E. A.; Yang, J. C. Critical Review: Effects of Complex Interactions on Structure and Dynamics of Supported Metal Catalysts. *J. Vac. Sci. Technol. A* **2014**, *32*, 020801.
11. Liao, L.; Zhang, Q.; Su, Z.; Zhao, Z.; Wang, Y.; Li, Y.; Lu, X.; Wei, D.; Feng, G.; Yu, Q.; et al. Efficient Solar Water-splitting Using a Nanocrystalline CoO Photocatalyst. *Nat. Nanotechnol* **2013**, *9*, 69–73.
12. Tyo, E. C.; Yin, C.; di Vece, M.; Qian, Q.; Kwon, G.; Lee, S.; Lee, B.; DeBartolo, J. E.; Seifert, S.; Winans, R. E.; et al. Oxidative Dehydrogenation of Cyclohexane on Cobalt Oxide (Co_3O_4) Nanoparticles: The Effect of Particle Size on Activity and Selectivity. *ACS Catal.* **2012**, *2*, 2409–2423.
13. Feng, H.; Elam, J. W.; Libera, J. A.; Pellin, M. J.; Stair, P. C. Oxidative Dehydrogenation of Cyclohexane over Alumina-Supported Vanadium Oxide Nanoliths. *J. Catal.* **2010**, *269*, 421–431.
14. Dummer, N. F.; Bawaked, S.; Hayward, J.; Jenkins, R.; Hutchings, G. J. Reprint of: Oxidative Dehydrogenation of Cyclohexane and Cyclohexene over Supported Gold, -Palladium Catalysts. *Catal. Today* **2011**, *160*, 50–54.
15. Sato, K. A. "Green" Route to Adipic Acid: Direct Oxidation of Cyclohexenes with 30% Hydrogen Peroxide. *Science* **1998**, *281*, 1646–1647.
16. Deng, Y.; Ma, Z.; Wang, K.; Chen, J. Clean Synthesis of Adipic Acid by Direct Oxidation of Cyclohexene with H_2O_2 over Peroxytungstate-Organic Complex Catalysts. *Green Chem.* **1999**, *1*, 275–276.
17. Schuchardt, U.; Cardoso, D.; Sercheli, R.; Pereira, R.; DaCruz, Rosenira S.; Guerreiro, M. C.; Mandelli, D.; Spinacé, E. V.; Pires, E. L. Cyclohexane Oxidation Continues to be a Challenge. *Appl. Catal., A* **2001**, *211*, 1–17.
18. Yin, Y.; Rioux, R. M.; Erdonmez, C. K.; Hughes, S.; Somorjai, G. A.; Alivisatos, A. P. Formation of Hollow Nanocrystals Through the Nanoscale Kirkendall Effect. *Science* **2004**, *304*, 711–714.
19. Cabot, A.; Puntes, V. F.; Shevchenko, E.; Yin, Y.; Balcells, L.; Marcus, M. A.; Hughes, S. M.; Alivisatos, A. P. Vacancy Coalescence during Oxidation of Iron Nanoparticles. *J. Am. Chem. Soc.* **2007**, *129*, 10358–10360.
20. Nakamura, R.; Tokozakura, D.; Nakajima, H.; Lee, J.-G.; Mori, H. Hollow Oxide Formation by Oxidation of Al and Cu Nanoparticles. *J. Appl. Phys.* **2007**, *101*, 074303–074307.
21. Nakamura, R.; Lee, J.-G.; Mori, H.; Nakajima, H. Oxidation Behaviour of Ni Nanoparticles and Formation Process of Hollow NiO. *Philos. Mag.* **2008**, *88*, 257–264.
22. Sutter, E.; Sutter, P. Size-Dependent Room Temperature Oxidation of In Nanoparticles. *J. Phys. Chem. C* **2012**, *116*, 20574–20578.
23. Ha, D.-H.; Moreau, L. M.; Honrao, S.; Hennig, R. G.; Robinson, R. D. The Oxidation of Cobalt Nanoparticles into Kirkendall-Hollowed CoO and Co_3O_4: The Diffusion Mechanisms and

Atomic Structural Transformations. *J. Phys. Chem. C* **2013**, *117*, 14303–14312.
24. Levitas, V. I.; Attariani, H. Mechanochemical Continuum Modeling of Nanovoid Nucleation and Growth in Reacting Nanoparticles. *J. Phys. Chem. C* **2012**, *116*, 54–62.
25. Fan, H. J.; Gösele, U.; Zacharias, M. Formation of Nanotubes and Hollow Nanoparticles Based on Kirkendall and Diffusion Processes: A Review. *Small* **2007**, *3*, 1660–1671.
26. Yin, Y.; Erdonmez, C. K.; Cabot, A.; Hughes, S.; Alivisatos, A. P. Colloidal Synthesis of Hollow Cobalt Sulfide Nanocrystals. *Adv. Funct. Mater.* **2006**, *16*, 1389–1399.
27. Chernavskii, P. A.; Pankina, G. V.; Zaikovskii, V. I.; Peskov, N. V.; Afanasiev, P. Formation of Hollow Spheres upon Oxidation of Supported Cobalt Nanoparticles. *J. Phys. Chem. C* **2008**, *112*, 9573–9578.
28. Varón, M.; Ojea-Jimenez, I.; Arbiol, J.; Balcells, L.; Martínez, B.; Puntes, V. F. Spontaneous Formation of Hollow Cobalt Oxide Nanoparticles by the Kirkendall Effect at Room Temperature at the Water–Air Interface. *Nanoscale* **2013**, *5*, 2429–2436.
29. Weststrate, C. J.; Hauman, M. M.; Moodley, D. J.; Saib, A. M.; Steen, E.; Niemantsverdriet, J. W. Cobalt Fischer–Tropsch Catalyst Regeneration: The Crucial Role of the Kirkendall Effect for Cobalt Redispersion. *Top. Catal.* **2011**, *54*, 811–816.
30. Thüne, P. C.; Weststrate, C. J.; Moodley, P.; Saib, A. M.; van de Loosdrecht, J.; Miller, J. T.; Niemantsverdriet, J. W. Studying Fischer–Tropsch Catalysts Using Transmission Electron Microscopy and Model Systems of Nanoparticles on Planar Supports. *Catal. Sci. Technol.* **2011**, *1*, 689–697.
31. Saib, A. M.; Moodley, D. J.; Ciobîc, I. M.; Hauman, M. M.; Sigwebela, B. H.; Weststrate, C. J.; Niemantsverdriet, J. W.; van de Loosdrecht, J. Fundamental Understanding of Deactivation and Regeneration of Cobalt Fischer–Tropsch Synthesis Catalysts. *Catal. Today* **2010**, *154*, 271–282.
32. Saib, A. M.; Gauché, J. L.; Weststrate, C. J.; Gibson, P.; Boshoff, J. H.; Moodley, D. J. Fundamental Science of Cobalt Catalyst Oxidation and Reduction Applied to the Development of a Commercial Fischer–Tropsch Regeneration Process. *Ind. Eng. Chem. Res.* **2014**, *53*, 1816–1824.
33. Lee, S.; di Vece, M.; Lee, B.; Seifert, S.; Winans, R. E.; Vajda, S. Oxidative Dehydrogenation of Cyclohexene on Size Selected Subnanometer Cobalt Clusters: Improved Catalytic Performance *via* Evolution of Cluster-Assembled Nanostructures. *Phys. Chem. Chem. Phys.* **2012**, *14*, 9336–9342.
34. Lee, S.; Lee, B.; Seifert, S.; Vajda, S.; Winans, R. E. Simultaneous Measurement of X-ray Small Angle Scattering, Absorption and Reactivity: A Continuous Flow Catalysis Reactor. *Nucl. Instrum. Methods, Phys. Res. A* **2011**, *649*, 200–203.
35. Ferguson, G. A.; Yin, C.; Kwon, G.; Tyo, E. C.; Lee, S.; Greeley, J. P.; Zapol, P.; Lee, B.; Seifert, S.; Winans, R. E.; et al. Stable Subnanometer Cobalt Oxide Clusters on Ultrananocrystalline Diamond and Alumina Supports: Oxidation State and the Origin of Sintering Resistance. *J. Phys. Chem. C* **2012**, *116*, 24027–24034.
36. Yin, C.; Zheng, F.; Lee, S.; Guo, J.; Wang, W.-C.; Kwon, G.; Vajda, V.; Wang, H.-H.; Lee, B.; DeBartolo, J.; et al. Size- and Support-Dependent Evolution of the Oxidation State and Structure by Oxidation of Subnanometer Cobalt Clusters. *J. Phys. Chem. A* **2014**, *118*, 8477–8484.
37. Kleibert, A.; Voitkans, A.; Meiwes-Broer, K.-H. Size-Dependent Alignment of Fe Nanoparticles upon Deposition onto W(110). *Phys. Rev. B* **2010**, *81*, 073412–073412–4.
38. Kleibert, A.; Voitkans, A.; Meiwes-Broer, K.-H. Reflection High Energy Electron Diffraction as a Tool in Cluster Deposition Experiments. *Phys. Stat. Sol. B* **2010**, *247*, 1048–1055.
39. Kitakami, O.; Sato, H.; Shimada, Y.; Sato, F.; Tanaka, M. Size Effect on the Crystal Phase of Cobalt Fine Particles. *Phys. Rev. B* **1997**, *56*, 13849–13854.
40. Kraus, W.; Nolze, G. POWDER CELL - a Program for the Representation and Manipulation of Crystal Structures and Calculation of the Resulting X-ray Powder Patterns. *J. Appl. Crystallogr.* **1996**, *29*, 301–303.
41. Goergen, S.; Yin, C.; Yang, M.; Lee, B.; Lee, S.; Wang, C.; Wu, P.; Boucher, M. B.; Kwon, G.; Seifert, S.; et al. Structure Sensitivity of Oxidative Dehydrogenation of Cyclohexane over FeO_x and Au/Fe_3O_4 Nanocrystals. *ACS Catal.* **2013**, *3*, 529–539.
42. Chen, Z. H.; Kim, C.; Zeng, X.-b.; Hwang, S. H.; Jang, J.; Ungar, G. Characterizing Size and Porosity of Hollow Nanoparticles: SAXS, SANS, TEM, DLS, and Adsorption Isotherms Compared. *Langmuir* **2012**, *28*, 15350–15361.
43. Chen, H.-J.; Li, S.-Y.; Liu, X.-J.; Li, R.-P.; Smilgies, D.-M.; Wu, Z.-H.; Li, Z. Evaluation on Pore Structures of Organosilicate Thin Films by Grazing Incidence Small-Angle X-ray Scattering. *J. Phys. Chem. B* **2009**, *113*, 12623–12627.
44. George, S. M. Atomic Layer Deposition: An Overview. *Chem. Rev.* **2010**, *110*, 111–131.
45. Puurunen, R. L.; Vandervorst, W. Island Growth as a Growth Mode in Atomic Layer Deposition: A Phenomenological Model. *J. Appl. Phys.* **2004**, *96*, 7686–7695.
46. Puurunen, R. L.; Vandervorst, W.; Besling, W. F. A.; Richard, O.; Bender, H.; Conard, T.; Zhao, C.; Delabie, A.; Caymax, M.; Gendt, S. d.; et al. Island Growth in the Atomic Layer Deposition of Zirconium Oxide and Aluminum Oxide on Hydrogen-terminated Silicon: Growth Mode Modeling and Transmission Electron Microscopy. *J. Appl. Phys.* **2004**, *96*, 4878–4889.
47. Sadasivan, S.; Bellabarba, R. M.; Tooze, R. P. Size Dependent Reduction-Oxidation-Reduction Behaviour of Cobalt Oxide Nanocrystals. *Nanoscale* **2013**, *5*, 11139–11146.
48. Ermoline, A.; Dreizin, E. L. Equations for the Cabrera–Mott Kinetics of Oxidation for Spherical Nanoparticles. *Chem. Phys. Lett.* **2011**, *505*, 47–50.
49. Cabrera, N.; Mott, N. F. Theory of the Oxidation of Metals. *Rep. Prog. Phys.* **1949**, *12*, 163–184.
50. Grajewski, V.; Fromm, E. Low-Temperature Oxidation of Metals. *Solid State Phenom.* **1991**, *15–16*, 337–400.
51. Díaz-Fernández, D.; Méndez, J.; Bomatí-Miguel, O.; Yubero, F.; Mossanek, R.; Abbate, M.; Domínguez-Cañizares, G.; Gutiérrez, A.; Tougaard, S.; Soriano, L. The Growth of Cobalt Oxides on HOPG and SiO_2 Surfaces: A Comparative Study. *Surf. Sci.* **2014**, *624*, 145–153.
52. Dureuil, V.; Ricolleau, C.; Gandais, M.; Grigis, C.; Lacharme, J.; Naudon, A. Growth and Morphology of Cobalt Nanoparticles on Alumina. *J. Cryst. Growth* **2001**, *233*, 737–748.
53. Vajda, S.; Lee, S.; Di Vece, M.; Lee, B.; Seifert, S.; Winans, R. E.; Ferguson, G. A.; Curtiss, L. A.; Greeley, J. P.; Qian, Q.; et al. Size- and Composition Optimized Sub-Nanometer and nm Size Catalysts for Low-Temperature Jet-Fuel Activation. *Prepr. Am. Chem. Soc., Div. Pet. Chem.* **2011**, *56*, 384–385.
54. Yang, Z.; Walls, M.; Lisiecki, I.; Pileni, M.-P. Unusual Effect of an Electron Beam on the Formation of Core/Shell (Co/CoO) Nanoparticles Differing by Their Crystalline Structures. *Chem. Mater.* **2013**, *25*, 2372–2377.
55. Yang, Z.; Yang, N.; Bergström, J.; Pileni, M.-P. Control of the Oxygen and Cobalt Atoms Diffusion Through Co Nanoparticles Differing by Their Crystalline Structure and Size. *Adv. Funct. Mater.* **2015**, *25*, 891–897.
56. Doan, N.; Kontturi, K.; Johans, C. Directing Oxidation of Cobalt Nanoparticles with the Capping Ligand. *J. Colloid Interface Sci.* **2010**, *350*, 126–131.
57. Jansson, J.; Low-Temperature, C. O. Oxidation over Co_3O_4/Al_2O_3. *J. Catal.* **2000**, *194*, 55–60.
58. Yu, Y.; Zhao, J.; Han, X.; Zhang, Y.; Qin, X.; Wang, B. Influence of Calcination and Pretreatment Conditions on the Activity of Co_3O_4 for CO oxidation. *Chin. J. Catal.* **2013**, *34*, 283–293.
59. Carlisle, J. Advanced Diamond Technologies, Inc., 2011–2013 http://www.thindiamond.com/index.php?cID=145.
60. Lee, S.; Molina, L. M.; López, M. J.; Alonso, J. A.; Hammer, B.; Lee, B.; Seifert, S.; Winans, R. E.; Elam, J. W.; Pellin, M. J.; et al. Selective Propene Epoxidation on Immobilized Au 6–10 Clusters: The Effect of Hydrogen and Water on Activity and Selectivity. *Angew. Chem.* **2009**, *121*, 1495–1499.
61. Molina, L. M.; Lee, S.; Sell, K.; Barcaro, G.; Fortunelli, A.; Lee, B.; Seifert, S.; Winans, R. E.; Elam, J. W.; Pellin, M. J.

Size-Dependent Selectivity and Activity of Silver Nanoclusters in the Partial Oxidation of Propylene to Propylene Oxide and Acrolein: A Joint Experimental and Theoretical Study. *Catal. Today* **2011**, *160*, 116–130.
62. Passig, J.; Meiwes-Broer, K.-H.; Tiggesbäumker, J. Collimation of Metal Nanoparticle Beams Using Aerodynamic Lenses. *Rev. Sci. Instrum.* **2006**, *77*, 093304–093304−5.
63. Bouwen, W.; Thoen, P.; Vanhoutte, F.; Bouckaert, S.; Despa, F.; Weidele, H.; Silverans, R. E.; Lievens, P. Production of Bimetallic Clusters by a Dual-Target Dual-Laser Vaporization Source. *Rev. Sci. Instrum.* **2000**, *71*, 54–58.
64. Harbich, W. 'Soft Landing' of Size-Selected Clusters in Chemically Inert Substrates. *Philos. Magn. B* **1999**, *79*, 1307–1320.
65. Heiz, U.; Schneider, W.-D. Nanoassembled Model Catalysts. *J. Phys. D: Appl. Phys.* **2000**, *33*, R85–R102.
66. Cheng, H.-P.; Landman, U. Controlled Deposition, Soft Landing, and Glass Formation in Nanocluster-Surface Collisions. *Science* **1993**, *260*, 1304–1307.
67. Watanabe, M.; Uchida, N.; Kanayama, T. Impact-Energy Dependence of Hydrogenated Si Cluster Deposition on Si(111)-(7 × 7). *Phys. Rev. B* **2000**, *61*, 7219–7222.
68. Getzlaff, M.; Kleibert, A.; Methling, R.; Bansmann, J.; Meiwes-Broer, K.-H. Mass-Filtered Ferromagnetic Alloy Clusters on Surfaces. *Surf. Sci.* **2004**, *566−568*, 332–336.
69. Popok, V. N.; Barke, I.; Campbell, E. E.; Meiwes-Broer, K.-H. Cluster-Surface Interaction: From Soft Landing to Implantation. *Surf. Sci. Rep.* **2011**, *66*, 347–377.
70. Flagan, R. C.; Lunden, M. M. Particle Structure Control in Nanoparticle Synthesis from the Vapor Phase. *Mater. Sci. Eng., Proc. Conf.* **1995**, *204*, 113–124.
71. Wegner, K.; Piseri, P.; Tafreshi, H. V.; Milani, P. Cluster Beam Deposition: a Tool for Nanoscale Science and Technology. *J. Phys. D: Appl. Phys.* **2006**, *39*, R439–R459.
72. Vandamme, N.; Janssens, E.; Vanhoutte, F.; Lievens, P.; van Haesendonck, C. Scanning Probe Microscopy Investigation of Gold Clusters Deposited on Atomically Flat Substrates. *J. Phys.: Condens. Matter* **2003**, *15*, S2983–S2999.
73. Lei, Y.; Mehmood, F.; Lee, S.; Greeley, J.; Lee, B.; Seifert, S.; Winans, R. E.; Elam, J. W.; Meyer, R. J.; Redfern, P. C.; et al. Increased Silver Activity for Direct Propylene Epoxidation via Subnanometer Size Effects. *Science* **2010**, *328*, 224–228.
74. Wyrzgol, S. A.; Schäfer, S.; Lee, S.; Lee, B.; di Vece, M.; Li, X.; Seifert, S.; Winans, R. E.; Stutzmann, M.; Lercher, J. A.; et al. Combined TPRx, In Situ GISAXS and GIXAS Studies of Model Semiconductor-Supported Platinum Catalysts in the Hydrogenation of Ethene. *Phys. Chem. Chem. Phys.* **2010**, *12*, 5585–5595.
75. Ilavsky, J.; Jemian, P. R. Irena: Tool Suite for Modeling and Analysis of Small-Angle Scattering. *J. Appl. Crystallogr.* **2009**, *42*, 347–353.
76. Cheng, L.; Yin, C.; Mehmood, F.; Liu, B.; Greeley, J.; Lee, S.; Lee, B.; Seifert, S.; Winans, R. E.; Teschner, D.; et al. Reaction Mechanism for Direct Propylene Epoxidation by Alumina-Supported Silver Aggregates: The Role of the Particle/Support Interface. *ACS Catal.* **2014**, *4*, 32–39.
77. Ravel, B.; Newville, M. ATHENA, ARTEMIS, HEPHAESTUS: Data Analysis for X-ray Absorption Spectroscopy Using IFEFFIT. *J. Synchrotron Radiat.* **2005**, *12*, 537–541.
78. Bartling, S.; Barke, I.; Sell, K.; Polei, S.; Oeynhausen, V. v.; Meiwes-Broer, K.-H. Structure of AuSi Nanoparticles on Si(111) from Reflection High-Energy Electron Diffraction and Scanning Tunneling Microscopy. *Eur. Phys. J. D* **2011**, *63*, 225–230.
79. Mahan, J. E. A. Review of the Geometrical Fundamentals of Reflection High-Energy Electron Diffraction with Application to Silicon Surfaces. *J. Vac. Sci. Technol. A* **1990**, *8*, 3692–3700.